공학석사 학위논문

Generative Adversarial Network based Quantitative Cone Beam CT for Bone Mineral Density

골밀도 측정을 위한 적대적생성신경망 기반 정량적 CBCT 측정

2021 년 8 월

서울대학교 대학원

응용바이오공학 전공

용 태 훈

골밀도 측정을 위한 적대적생성신경망 기반 정량적 CBCT 측정

지도교수 이 원 진

이 논문을 공학석사 학위논문으로 제출함

2021 년 6 월

서울대학교 대학원

응용바이오공학 전공

용 태 훈

용태훈의 공학석사 학위논문을 인준함

2021 년 7 월

위 원 장 _____ 허 민 석 _____

부위원장 _____ 이 원 진 _____

위　　원 _____ 예 성 준 _____

ABSTRACT

Generative Adversarial Network based Quantitative Cone Beam CT for Bone Mineral Density

Tae-Hoon Yong

Department of Applied Bioengineering

Graduate School of Convergence Science and Technology

Seoul National University

The purpose of this study was to directly and quantitatively measure BMD from Cone-beam CT (CBCT) images by enhancing the linearity and uniformity of the bone intensities based on a hybrid deep-learning model (QCBCT-NET) of combining the generative adversarial network (Cycle-GAN) and U-Net, and to compare the bone images enhanced by the QCBCT-NET with those by Cycle-GAN and U-Net. We used two phantoms of human skulls

encased in acrylic, one for the training and validation datasets, and the other for the test dataset. We proposed the QCBCT-NET consisting of Cycle-GAN with residual blocks and a multi-channel U-Net using paired training data of quantitative CT (QCT) and CBCT images. The BMD images produced by QCBCT-NET significantly outperformed the images produced by the Cycle-GAN or the U-Net in mean absolute difference (MAD), peak signal to noise ratio (PSNR), normalized cross-correlation (NCC), structural similarity (SSIM), and linearity when compared to the original QCT image. The QCBCT-NET improved the contrast of the bone images by reflecting the original BMD distribution of the QCT image locally using the Cycle-GAN, and also spatial uniformity of the bone images by globally suppressing image artifacts and noise using the two-channel U-Net. The QCBCT-NET substantially enhanced the linearity, uniformity, and contrast as well as the anatomical and quantitative accuracy of the bone images, and demonstrated more accuracy than the Cycle-GAN and the U-Net for quantitatively measuring BMD in CBCT.

Keywords: Bone mineral density, Quantitative CBCT, Deep learning, Generative adversarial network (GAN), U-Net

Student Number: 2019-23327

CONTENTS

LIST OF FIGURES

LIST OF TABLES

LIST OF ABBREVIATIONS

Full Name	Abbreviations
Bone mineral density	BMD
Hounsfield Units	HU
Quantitative CT	QCT
Multi-detector CT	MDCT
Cone-beam CT	CBCT
Generative Adversarial Network	GAN
Calibrated CBCT	CAL_CBCT
Mean Absolute Difference	MAD
Structural Difference	SSIM
Peak Signal to Noise Ratio	PSNR
Normalized Cross Correlation	NCC
Mean Squared Error	MSE
Spatial Nonuniformity	SNU
Statistical Package for Social Sciences	SPSS

INTRODUCTION

Trabecular bone density, a determinant of bone strength, is important for the diagnosis of bone quality in bone diseases [1, 2]. Bone mineral density (BMD) measurements are a direct method of estimating human bone mass for diagnosing osteoporosis and predicting future fracture risk [3, 4]. Generally, volumetric BMD can be assessed quantitatively through the calibration of Hounsfield Units (HU) in CT, which is a method known as quantitative CT (QCT) [5, 6]. The multi-detector CT (MDCT) with rapid acquisition of 3D volume images enables QCT to be applied to clinically important sites for assessing BMD [7].

For dental implant treatment, precise in vivo measurement of alveolar bone quality is very important in determining the primary stability of dental implants [8]. Therefore, the alveolar bone quality of the implant site needs to be measured before surgery to determine whether the bone mineral density (BMD) is sufficient to support the implant [9]. Recently, cone-beam CT (CBCT) systems have been widely used for dental treatment and planning as they offer many advantages over MDCTs, including a lower radiation dose to

the patient, shorter acquisition times, better resolution, and greater detail [10-15]. However, the voxel intensity values in CBCT systems are arbitrary, and do not allow for the assessment of bone quality as the systems do not correctly show HUs [16-20]. The ability of the CBCT to assess the bone density is limited as the HUs derived from CBCT data is clearly different from that of MDCT data [5, 17-19, 21]. Several studies have been performed to resolve the discrepancy in HUs between MDCT and CBCT data [15-17, 22]. Some studies investigated the relationship between CBCT voxel intensity values and MDCT HUs using a BMD calibration phantom with material inserts of different attenuation coefficients [17, 23-27]. These studies showed that the use of the phantoms in CBCT scanners would be difficult for correlating CBCT voxel intensities with HUs because of the non-uniformity of the measurements and the nonlinear relationship between CBCT voxel intensities and HUs [15].

CBCTs have also been widely used for accurate patient setups in image-guided radiation therapy [28]. Many methods for correcting CBCT images with high quality have been proposed to produce quantitative CBCTs in the radiation therapy field, which do not require a calibration phantom during an object scan. These methods can be classified as hardware corrections such

as anti-scatter grids, and model-based methods using Monte Carlo techniques to model the scatter to CBCT projections [29-34]. Recently, the generative adversarial network (GAN), a deep neural network model, has shown state-of-the-art performance in many image processing tasks [28, 35, 36]. The GAN is composed of two networks trained simultaneously with one focused on image generation and the other on discrimination. The GAN has the capability of data generation without explicitly modelling the probability density function [37]. In one study, a deep learning-based method using a modified GAN improved image quality for generating corrected CBCT images, which integrated a residual block concept into a Cycle-GAN framework [38]. Moreover, the U-Net model of U-shape encoder-decoder architecture is widely applied in biomedical image segmentation, image denoising [39-41], and image synthesis [42-44]. The U-Net based approach could efficiently synthesize artifact-suppressed CT-like CBCT images from CBCT images containing global scattering and local artifacts [43, 44].

To date, these deep learning-based studies have mainly focused on the improvement in voxel values of the soft tissues in CBCT images. As far as we know, no previous studies have quantitatively measured BMD from CBCT

images through the improvement of the bone image using deep learning. We hypothesized that a deep learning-based method could generate QCT-like CBCT images from CBCT images for directly measuring BMD by learning the pixel-wise mapping between QCT and CBCT images. The purpose of this study was to directly and quantitatively measure BMD from CBCT images by enhancing the linearity and uniformity of the bone intensities based on a hybrid deep-learning model (QCBCT-NET) of combining the generative adversarial network (Cycle-GAN) and U-Net, and to compare the bone images enhanced by the QCBCT-NET with those by Cycle-GAN and U-Net.

MATERIALS AND METHODS

Data Acquisition and Preparation

We used two phantoms of human skulls encased in acrylic articulated for medical use (Erler Zimmer Co., Lauf, Germany), one with and the other without metal restorations causing streak artifacts (Figure 1(a)). The phantoms have been used in our previous studies [45-48]. The images of the phantoms were obtained with a MDCT (Somatom Sensation 10, Siemens AG, Erlangen, Germany) and a CBCT (CS 9300, Carestream Health, Inc., Rochester, US), respectively. We acquired the CT images with voxel sizes of $0.469 \times 0.469 \times 0.5$ mm^3, dimensions of 512×512 pixels, and 16 bit depth under condition of 120 kVp and 130 mA, while the CBCT images were obtained with voxel sizes of $0.3 \times 0.3 \times 0.3$ mm^3, dimensions of 559×559 pixels, and 16 bit depth under conditions combined from 80 or 90 kVp and 8 or 10 mA (Table 1). In addition, CT and CBCT images of a BMD calibration phantom (QRM-BDC Phantom 200 mm length, QRM GmbH, Moehrendorf, Germany) with calcium hydroxyapatite inserts of three densities (0 (water), 100, and 200 mg/cm^3) were also obtained under the same condition (Figure 1(b), Figure 2). The CT images

of the skull phantoms were then converted into quantitative CT (QCT) images

based on Hounsfield Units (HU) by linear calibration using the CT images of

the BMD calibration phantom (Figure 3(a)). The CBCT images of the skull

phantoms were also converted into calibrated CBCT (CAL_CBCT) images

using the corresponding images of the BMD calibration phantom for

comparisons with deep learning results afterwards (Figure 3(b)).

Table 1. The Technical factors for MDCT and CBCT.

Technical factor	MDCT	CBCT
Manufacturer	Somatom Sensation 10, Siemens AG, Erlangen, Germany	CS 9300, Carestream Health, Inc., Rochester, US
Voxel sizes	$0.469 \times 0.469 \times 0.5$ mm^3	$0.3 \times 0.3 \times 0.3$ mm^3
Dimensions	512×512 pixels	559×559 pixels
Depth	16 bit	16 bit
Kilovoltage	120 kVp	80 or 90 kVp
Tube current-time product	130 mA	8 or 10 mA
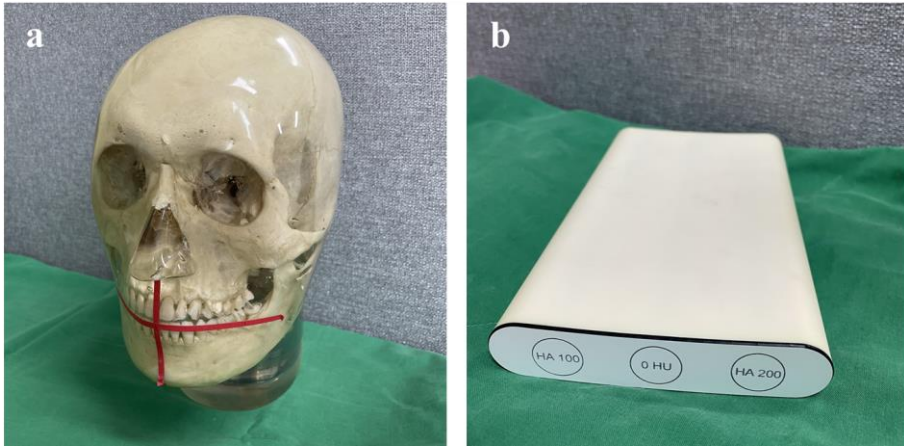
Figure 1. (a) A phantom of human skulls encased in acrylic articulated for medical use, and (b) a BMD calibration phantom.
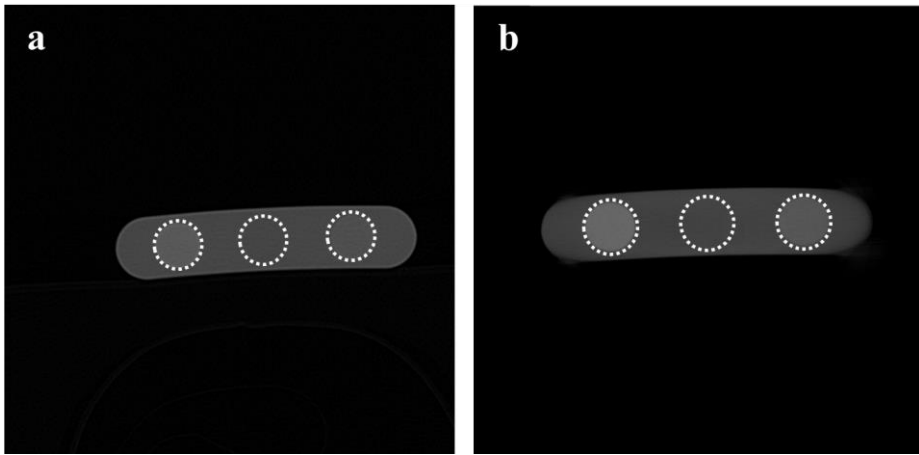
Figure 2. (a) MDCT, and (b) CBCT images of BMD calibration phantom with calcium hydroxyapatite inserts of three densities (0 (center circle), 100 (right circle), and 200 (left circle) mg/cm^3).
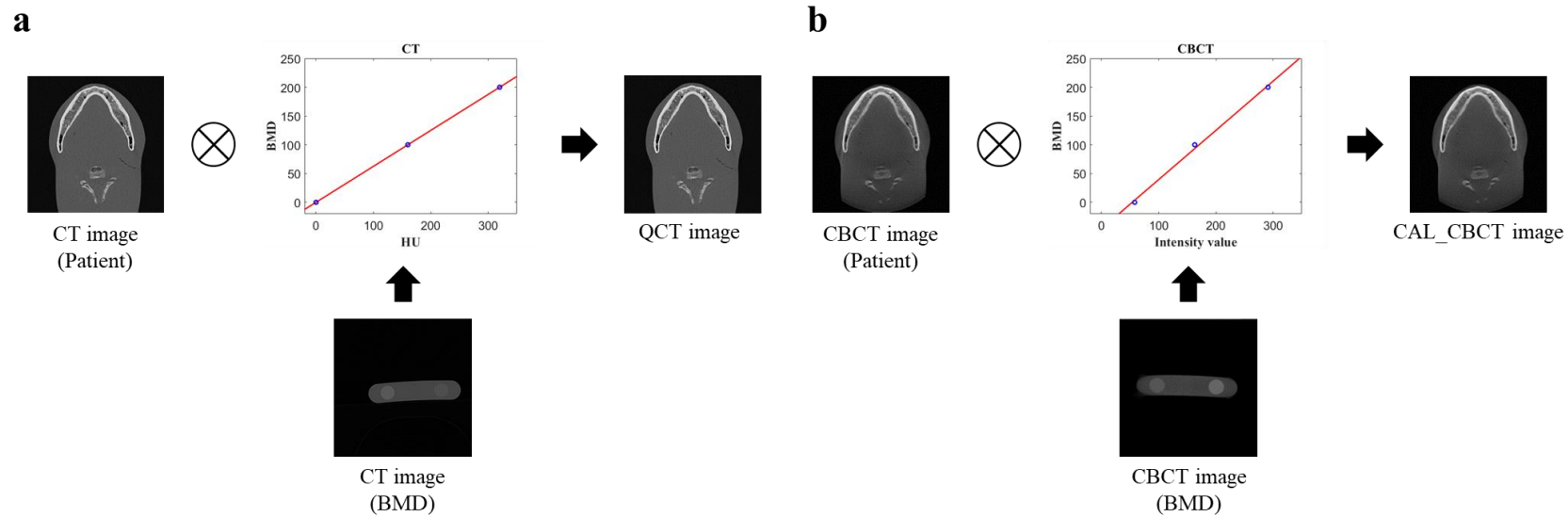
Figure 3. The quantitative CT (QCT) and calibrated CBCT (CAL_CBCT) images based on Hounsfield Units (HU) by linear calibration using the CT images of the BMD calibration phantom.

The CT image for the skull phantom was matched to the CBCT image by paired-point registration using a software (3D Slicer, MIT, Massachusetts, US), where the six landmarks were localized manually at the vertex on the lateral incisors, the buccal cusps of the first premolars, and the distobuccal cusps of the first molars [49] (Figure 4). The matched CT and CBCT images consisting of a matrix of 559×559×264 pixels were cropped at the maxillomandibular region, and then resized to images of 256×256×200 pixels (Figure 5). To avoid adverse impacts from non-anatomical regions during training, binary masks were applied to the CT and CBCT images to separate the maxillomandibular region from the non-anatomical regions [44] (Figure 6). The binary mask images were generated by using thresholding and morphological operations. The edges of anatomical regions were extracted by applying a local range filter to the paired CBCT and CT images [50], and the morphological operations of opening and flood fill were applied to the binarized edges obtained by thresholding to remove small blobs and fill the inner area. The corresponding CBCT and CT images were multiplied by the intersection of the two binary masks from CBCT and CT images. The voxel

values outside the masked region were replaced with Hounsfield Units (HUs) of -1000.

For deep learning, we prepared the 800 pairs of axial slice images for QCT and CBCTs from the skull phantom without metal restorations for the training and validation datasets (obtained under four conditions combined from 80 or 90 kVp, and 8 or 10 mA), and independently, another 400 pairs for QCT and CBCTs from the skull phantom with metal restorations for the test dataset (obtained under two conditions of 80 kVp and 8 mA, and 90 kVp and 10 mA) (Table 2).

Table 2. The Dataset configurations.

	MDCT (slices)	CBCT (slices)
Training and validation dataset	200	800
Test dataset	200	400
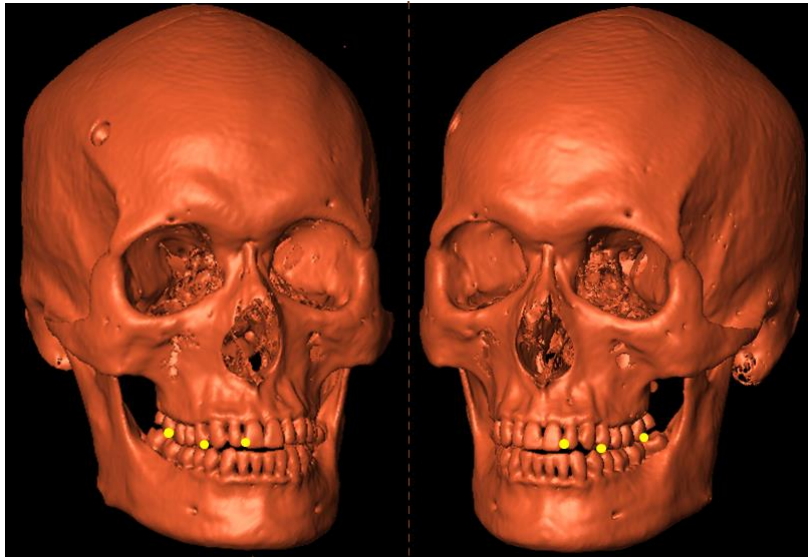
Figure 4. The six landmarks (yellow dots) localized at the vertex on the lateral incisors, the buccal cusps of the first premolars, and the distobuccal cusps of the first molars for paired-point registration of CT and CBCT images.
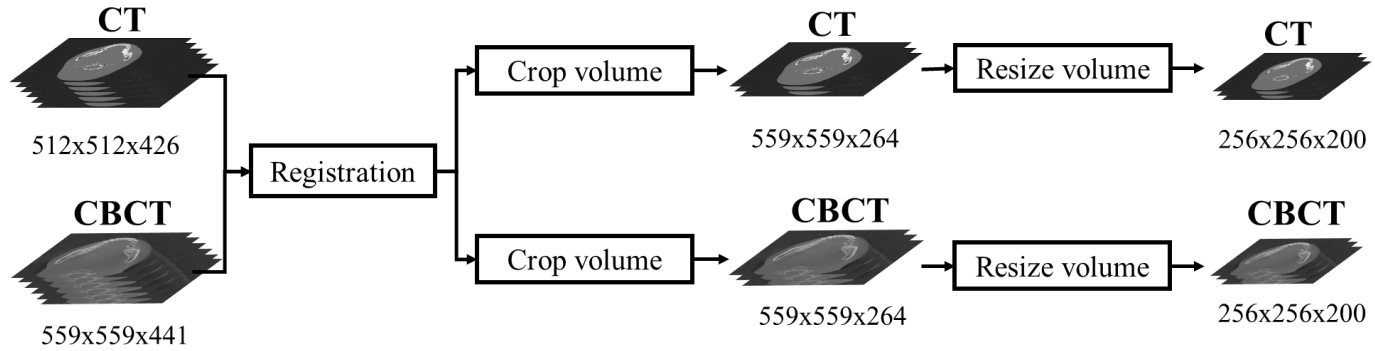
Figure 5. The matched CT and CBCT images cropped and resized at the maxillomandibular region.
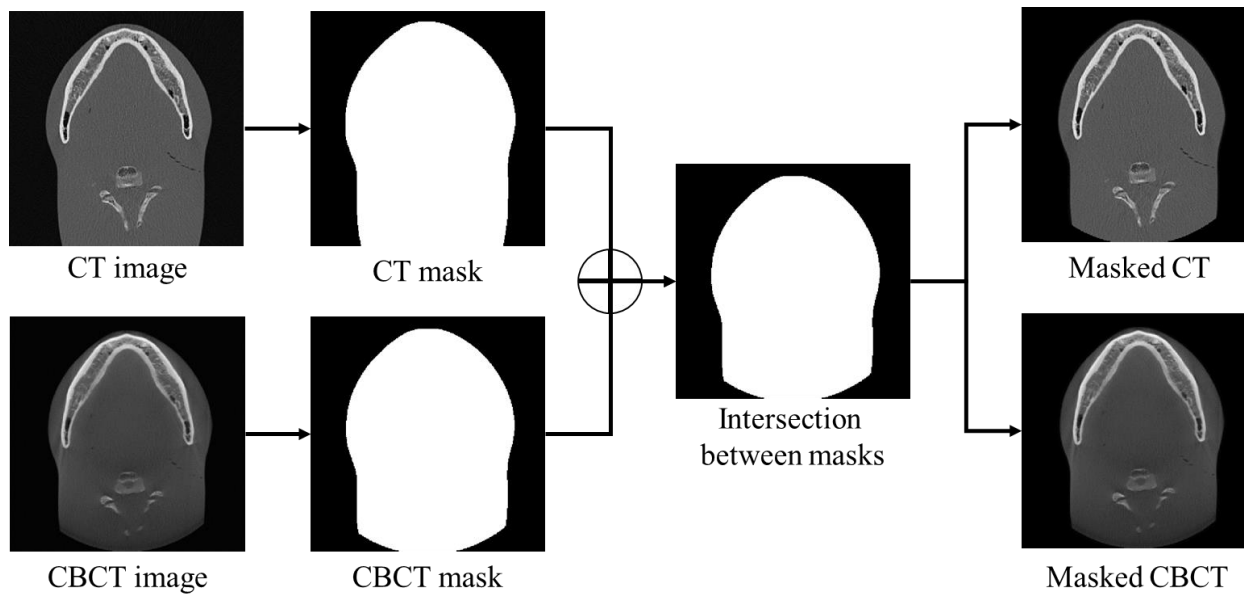
Figure 6. Binary masks applied to the CT and CBCT images to separate the maxillomandibular region from the non-anatomical regions.

Hybrid Deep-Learning Model (QCBCT-NET) for Quantitative CBCT images

We designed a hybrid deep-learning architecture (QCBCT-NET) consisting of Cycle-GAN and U-Net to generate QCT-like images from the conventional CBCT images (Figure 7), and also the Cycle-GAN and the U-Net with the same architecture with QCBCT-NET, respectively, for performance comparisons. We implemented Cycle-GAN with the residual blocks [38] combined with a multi-channel U-Net model using paired training data. The CycleGAN architecture contained two generators for yielding the CBCT to QCT (G_(CBCT→QCT)) and QCT to CBCT (G_(QCT→CBCT)) mappings, and two discriminators for distinguishing between real (D_QCT) and generated (D_CBCT) images. We adopted a ResNet architecture with nine residual blocks for the generators, and a PatchGAN of 70 × 70 patch for the discriminators.

The Cycle-GAN model was optimized using two part loss functions consisting of an adversarial loss and a cycle consistency loss [36]. The adversarial loss function relied on the output of the discriminators, which were defined as:

$$L_{ADV}(G_{CBCT \to QCT}) = D_{QCT}(I_{QCT})^2 + \left(D_{QCT}\left(G_{CBCT \to QCT}(I_{CBCT})\right) - 1\right)^2,$$

$$L_{ADV}(G_{QCT \to CBCT}) = D_{CBCT}(I_{CBCT})^2 + \left(D_{CBCT}\left(G_{QCT \to CBCT}(I_{QCT})\right) - 1\right)^2,$$

where I_{CBCT} was the CBCT image, and I_{QCT}, the QCT image.

To avoid mode collapse issues, we added a cycle consistency loss that reduced the space of mapping functions. The cycle consistency loss was defined as:

$$L_{CYC} = \left|G_{QCT \to CBCT}\left(G_{CBCT \to QCT}(I_{CBCT})\right) - I_{CBCT}\right| + \left|G_{CBCT \to QCT}\left(G_{QCT \to CBCT}(I_{QCT})\right) - I_{QCT}\right|,$$

where I_{CBCT} was the CBCT image, and I_{QCT}, the QCT image.

Finally, the loss function of Cycle-GAN was defined as:

$$L_{GAN} = L_{ADV}(G_{CBCT \to QCT}) + L_{ADV}(G_{QCT \to CBCT}) + \lambda L_{CYC},$$

where λ controlled the relative importance of the adversarial losses, and the used value of λ was 10.
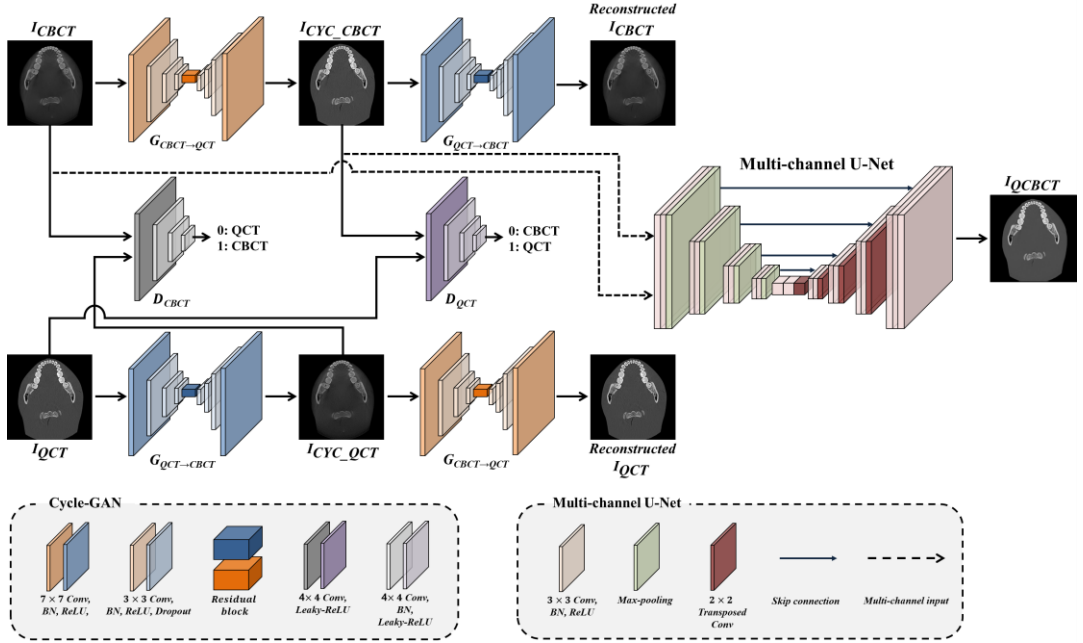
Figure 7. The QCBCT-NET architecture combining Cycle-GAN and the multi-channel U-net. The Cycle-GAN consisted of two generators of $G_{CBCT \rightarrow QCT}$, and $G_{QCT \rightarrow CBCT}$, and two discriminators of D_{CBCT}, and D_{QCT}. In the generators, the convolution block consisted of 7×7 and 3×3 convolution layers with batch normalization and ReLU activation, and residual blocks were embedded in the middle of the down-sampling and up-sampling layers. In discriminators, the convolution block consisted of 4×4 convolution layers with batch normalization and leaky ReLU activation followed by down-sampling layers. The multi-channel U-Net had two-channel inputs of CBCT and corresponding CYC_CBCT images, consisting of 3×3 convolution layers with batch normalization and ReLU activation, and had skip connections at each layer level. Max-pooling was used for down-sampling and transposed convolution was used for up-sampling.

To generate QCBCT images, we implemented the multi-channel U-Net with four skip-connections between an encoder and a decoder at each resolution level using the two-channel inputs consisting of the original CBCT image, and the corresponding output of the Cycle-GAN. The multi-channel U-Net was optimized by the loss function consisting of the mean absolute difference (MAD) and structural difference (SSIM) between QCBCT and QCT images [43], which were defined as:

$$L_{MAD} = \left| I_{QCT} - I_{QCBCT} \right|, \quad L_{\text{SSIM}} = \frac{\left(2\mu_{QCT}\mu_{QCBCT} + C_1 \right)\left(2\sigma_{QCT\,QCBCT} + C_2 \right)}{\left(\mu^2_{QCT} + \mu^2_{QCBCT} + C_1 \right)\left(\sigma^2_{QCT} + \sigma^2_{QCBCT} + C_2 \right)},$$

where I_{QCBCT} was the QCBCT image, I_{QCT}, the QCT image, μ, mean, σ^2, variance, and C_1 and C_2, variables to stabilize the division with weak denominators.

Finally, the loss function of the multi-channel U-Net was defined as:

$$L_{UNet} = (1 - \alpha)L_{\text{MAD}} + \alpha(1 - L_{\text{SSIM}}),$$

where the used value of α was 0.6.

The deep learning model was trained and tested using a workstation with four GPUs of Nvidia GeForce GTX 1080 Ti and 11 GB of VRAM. The

Cycle-GAN model was trained by the Adam optimizer with a mini-batch size of 8 and epoch number of 200. For the first 100 epochs, the learning rate was maintained at 0.0002, and decreased linearly approaching zero for the next 100 epochs. The U-Net model was trained by the Adam optimizer with a mini-batch size of 8 and epoch number of 200. The learning rate was set to 0.0001 with momentum terms of 0.9 to stabilize the training.

To compare the performance of measuring BMD from QCBCT images produced by the QCBCT-NET with those by the Cycle-GAN or the U-Net, we used the same settings with QCBCT-NET for the Cycle-GAN and the U-Net, and trained the networks with only CBCT as the network input, respectively.

Evaluation of Quantitative CBCT Images for Measuring BMD

To quantitatively evaluate the performance of measuring BMD from CBCT images by the different deep learning models, we compared the mean absolute difference (MAD), peak signal to noise ratio (PSNR), normalized cross correlation (NCC), and structural similarity (SSIM) between the original QCT image (the ground truth), and QCBCT image produced by QCBCT-NET, CYC_CBCT image produced by Cycle-GAN, U_CBCT image produced by U-NET, and CAL_CBCT image produced by only calibration for the CBCT image of the test dataset obtained under two scanning conditions. The MAD was defined as the mean of the absolute differences between the intensities of the QCT and CBCT images, the PSNR as the logarithm of the maximum possible intensity (MAX) over the root mean squared error (MSE) between the intensities of the QCT and CBCT images ($PSNR = 20 \times log_{10} \frac{MAX}{\sqrt{MSE}}$), the NCC as the multiplication between the intensities of the QCT and CBCT images divided by each standard deviation ($NCC = \frac{(I_{QCT}-\mu_{QCT})(I_{CBCT}-\mu_{CBCT})}{\sigma_{QCT}\sigma_{CBCT}}$), and SSIM the same as described above. The quantitative measurements in each slice were averaged over the whole maxilla and mandible. The higher values of PSNR, SSIM, and NCC, and the lower MAE indicated better performance for

22

BMD measurement from CBCT images.

Spatial nonuniformity (SNU) of the CBCT images was measured as the absolute difference between the maximum and the minimum of the BMD values in rectangular ROIs around the maxilla and mandible. To evaluate the linearity of BMD measurements in the CBCT images, we analyzed the relationship between the voxel intensities of the QCT (the ground truth) and CBCT images through a linear regression of the voxel intensities (Slope, slope of linear regression) at the maxilla and mandible, respectively. The lower SNU, and the higher Slope indicated better performance for BMD measurement from CBCT images. We also performed the Bland–Altman analysis to analyze the bias and agreement limits of the BMD between QCT (the ground truth) and CBCT images at the maxilla and mandible.

We compared the performances between QCBCT and other CBCT images at the maxilla and mandible under two conditions of 80 kVp and 8 mA, and 90 kVp and 10 mA with respect to the variations of BMD values of a bone depending on their relative positions [51], and those affected by scanning conditions. Paired two-tailed t-tests were used (SPSS v26, SPSS Inc., Chicago, IL, USA) to compare the quantitative performances between QCBCT and

CYC_CBCT images, between QCBCT and U_CBCT images, and between

QCBCT and CAL_CBCT images. Statistical significance level was set at 0.01.

RESULTS

Table 3 summarizes the means of the quantitative performance results for measuring BMD from QCBCT images produced by QCBCT-NET, CYC_CBCT produced by Cycle-GAN, U_CBCT produced by U-NET, and CAL_CBCT produced by calibration for the CBCT images of test datasets acquired for the skull phantom with metal restorations under conditions of 80 kVp and 8 mA, and 90 kVp and 10 mA. The BMD images of QCBCTs significantly outperformed the CYC_CBCT and U_CBCT images in MAD, PSNR, SSIM, and NCC at both the maxilla and mandible area when compared to the original QCT images (Table 3). All performances from the QCBCT images exhibited significant differences with those from the CYC_CBCT or U_CBCT images at the maxilla and mandible ($p < 0.01$) except for the SNU from the U_CBCT ($p = 0.04$) (Table 3). Compared to the BMD measurements from the CYC_CBCT image, the BMD from the QCBCT showed increases of 38% MAD, 20% PSNR, 45% SSIM, 40% NCC, 80% SNU, and 84% Slope at the maxilla, and 39% MAD, 20% PSNR, 50% SSIM, 40% NCC, 47% SNU, and 102% Slope at the mandible for CBCT images under condition of 80 kVp

and 8 mA (Table 4). Compared to the BMD measurement from the U_CBCT image, increases of 59% MAD, 41% PSNR, 112% SSIM, 58% NCC, -17% SNU, and 167% Slope at the maxilla, and 49% MAD, 33% PSNR, 81% SSIM, 54% NCC, -25% SNU, and 142% Slope at the mandible for CBCT images under condition of 80 kVp and 8 mA (Table 4). Under the higher dose condition of 90 kVp and 10 mA, the BMD from the QCBCT also showed higher performances at both the maxilla and mandible compared to the CYC_CBCT and U_CBCT (Table 4). Therefore, the BMDs from the QCBCT demonstrated more accuracy than those from the CYC_CBCT and U_CBCT without regard to relative positions of the bone, or effects from different scanning conditions.

Figure 8 shows the axial slices of the BMD images from the original QCT, QCBCT, CYC_CBCT, U_CBCT, and CAL_CBCT at the maxilla and mandible. As shown in the subtraction images in Figure 8, the BMD image quality of the QCBCTs for the two regions exhibited substantial improvement over those of CYC_CBCT, U_CBCT, and CAL_CBCT in terms of BMD (voxel intensity) differences compared to the original QCT images. The large differences around the teeth and dense bone of higher voxel intensities (BMD)

seen in the CAL_CBCT were more reduced in the QCBCT than in the CYC_CBCT or U_CBCT images.

Figure 9 shows the BMD (voxel intensity) profiles that were acquired along the dental arch at the maxilla and mandible in the QCT and CBCT images as shown in Figure 8. The BMD profile from the QCBCT images more closely reflected the original QCT than the CYC_CBCT and U_CBCT images with higher correlations with the QCT than other CBCT images, although the dental implant and restoration showed higher voxel intensities compared to other anatomical structures (Figure 9). Therefore, the QCBCT image exhibited more improved structural preservation and edge sharpness of the bone than the CYC_CBCT and U_CBCT images at both the maxilla and mandible. The BMD distribution of the QCBCT also more closely restored the original QCT than that of the CYC_CBCT and U_CBCT images in an axial slice at the maxilla and mandible (Figure 10). The linear relationship between the QCT and QCBCT images showed more contrast and correlation than that between QCT and other CBCT images with the larger slope and better goodness of fit (Figure 11). The Bland-Altman plot between QCT and QCBCT images also showed higher linear relationships and better agreement limits than that between QCT

and other CBCT images (Figure 12). Therefore, the QCBCT images showed more improvement in preservation for the original distribution and linear relationship of the BMD values compared to CYC_CBCT and U_CBCT images.

Table 3. Quantitative performance of CBCT images produced by QCBCT-NET, Cycle-GAN, U-Net, and CAL_CBCT compared to the original QCT images for measuring BMD values at the maxilla (1-81 slices) and mandible (82-200 slices) for test datasets under conditions of 80 kVp and 8 mA, and 90 kVp and 10 mA. MAD: mean absolute difference; PSNR: peak signal to noise ratio; SSIM: structural similarity; NCC: normalized cross correlation; SNU: spatial nonuniformity; Slope: slope of linear regression between the voxel intensities. (Mean ± SD, *: significant difference ($p < 0.01$) between QCBCT-NET and U-Net, †: ($p < 0.01$) between QCBCT-NET and Cycle-GAN, and ‡: ($p < 0.01$) between QCBCT-NET and CAL_CBCT.

		Maxilla						Mandible					
		MAD	PSNR	SSIM	NCC	SNU	Slope	MAD	PSNR	SSIM	NCC	SNU	Slope
80 kVp 8 mA	QCBCT-NET	203.45±27.24[*†‡]	23.87±1.34[*†‡]	0.87±0.02[*†‡]	0.87±0.02[*†‡]	15.60±7.85[‡]	0.83±0.04[*†‡]	190.79±34.46[*‡]	24.58±1.39[*†‡]	0.87±0.07[*†‡]	0.88±0.06[*†‡]	21.85±7.72[‡]	0.85±0.16[*†‡]
	Cycle-GAN (p-value)	328.91±55.12 (0.00)	19.94±1.63 (0.00)	0.60±0.07 (0.00)	0.62±0.08 (0.00)	79.04±13.48 (0.00)	0.45±0.06 (0.00)	313.14±58.68 (0.00)	20.52±1.42 (0.00)	0.58±0.08 (0.00)	0.63±0.11 (0.00)	41.59±10.56 (0.00)	0.42±0.09 (0.00)
	U-Net (p-value)	493.91±45.14 (0.00)	16.93±0.86 (0.00)	0.41±0.07 (0.00)	0.55±0.08 (0.00)	13.39±3.22 (0.04)	0.31±0.06 (0.00)	371.00±36.81 (0.00)	18.54±1.31 (0.00)	0.48±0.08 (0.00)	0.57±0.12 (0.00)	17.54±2.84[*] (0.00)	0.35±0.08 (0.00)
	CAL_CBCT (p-value)	592.40±53.76 (0.00)	15.63±0.80 (0.00)	0.31±0.08 (0.00)	0.61±0.08 (0.00)	69.30±15.05 (0.00)	0.26±0.06 (0.00)	491.44±95.51 (0.00)	17.33±1.52 (0.00)	0.40±0.05 (0.00)	0.62±0.11 (0.00)	39.19±11.14 (0.00)	0.30±0.08 (0.00)
80 kVp 8 mA	QCBCT-NET	265.4±63.41[*†‡]	21.92±1.98[*†‡]	0.79±0.02[*†‡]	0.84±0.02[*†‡]	27.09±38.42[‡]	0.62±0.04[*†‡]	236.25±68.62[*†‡]	22.98±2.36[*†‡]	0.79±0.08[*†‡]	0.80±0.15[*†‡]	15.87±4.24[‡]	0.66±0.11[*†‡]
	Cycle-GAN (p-value)	296.82±53.03 (0.00)	21.08±1.39 (0.00)	0.72±0.04 (0.00)	0.76±0.05 (0.00)	68.91±47.76 (0.00)	0.55±0.05 (0.00)	288.28±61.30 (0.00)	21.38±2.17 (0.00)	0.69±0.07 (0.00)	0.71±0.14 (0.00)	36.22±8.96 (0.00)	0.53±0.09 (0.00)
	U-Net (p-value)	474.15±52.87 (0.00)	17.40±0.88 (0.00)	0.50±0.06 (0.00)	0.68±0.09 (0.00)	16.02±30.39[*] (0.00)	0.38±0.04 (0.00)	370.59±104.16 (0.00)	19.66±2.68 (0.00)	0.57±0.07 (0.00)	0.67±0.14 (0.00)	12.80±4.08[*] (0.00)	0.40±0.06 (0.00)
	CAL_CBCT (p-value)	661.48±61.59 (0.00)	14.87±0.78 (0.00)	0.29±0.08 (0.00)	0.75±0.05 (0.00)	52.71±23.00 (0.00)	0.31±0.05 (0.00)	573.25±93.37 (0.00)	16.15±1.42 (0.00)	0.37±0.08 (0.00)	0.72±0.13 (0.00)	72.44±30.46 (0.00)	0.31±0.06 (0.00)

Table 4. Percentage increases of QCBCT-NET performance compared to Cycle-GAN and U-Net for measuring BMD values at the maxilla (1-81 slices) and mandible (82-200 slices) for CBCT images of test datasets under conditions of 80 kVp and 8 mA, and 90 kVp and 10 mA. MAD: mean absolute difference; PSNR: peak signal to noise ratio; SSIM: structural similarity; NCC: normalized cross correlation; SNU: spatial nonuniformity; Slope: slope of linear regression between the voxel intensities.

		Maxilla (%)						Mandible (%)					
		MAD	PSNR	SSIM	NCC	SNU	Slope	MAD	PSNR	SSIM	NCC	SNU	Slope
80 kVp 8 mA	vs. Cycle-GAN	38.14	19.71	45.00	40.32	80.26	84.44	39.07	19.79	50.00	39.68	47.46	102.38
	vs. U-Net	58.81	40.99	112.20	58.18	-16.50	167.74	48.57	32.58	81.25	54.39	-24.57	142.86
90 kVp 10 mA	vs. CycleGAN	10.59	3.98	9.72	10.53	59.10	12.73	17.69	7.48	14.49	12.68	56.18	24.53
	vs. U-Net	44.03	25.98	58.00	23.53	-73.47	63.16	36.40	16.89	38.60	19.40	-23.98	65.00
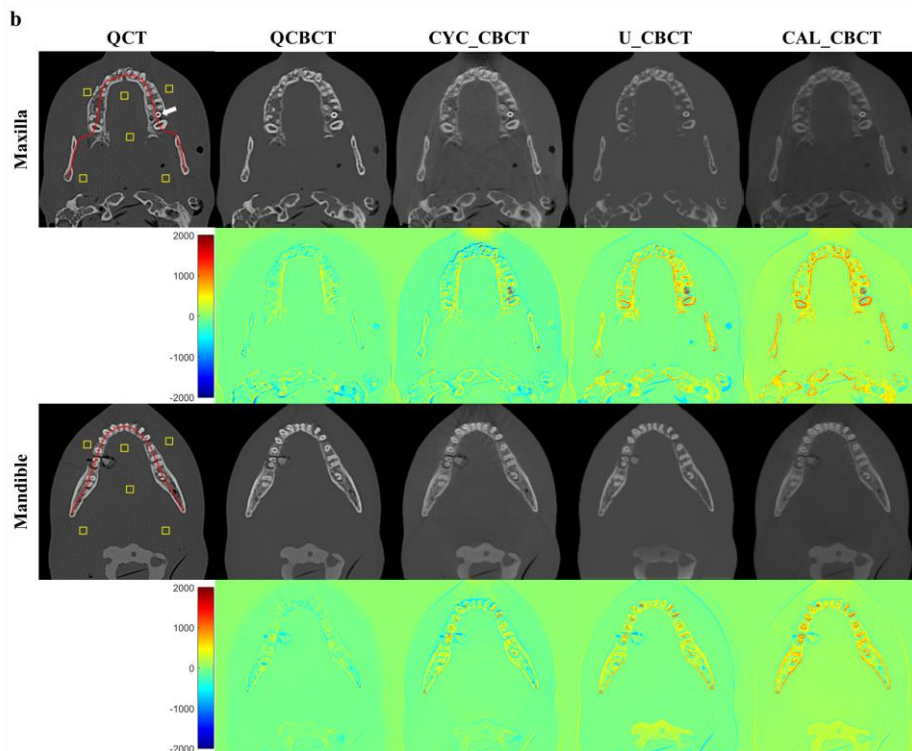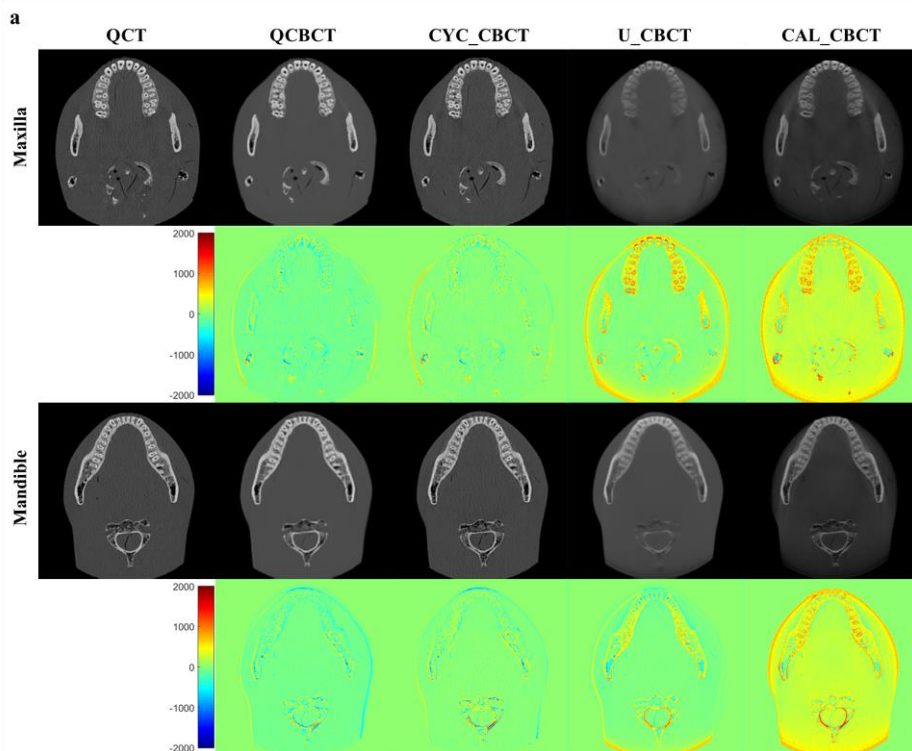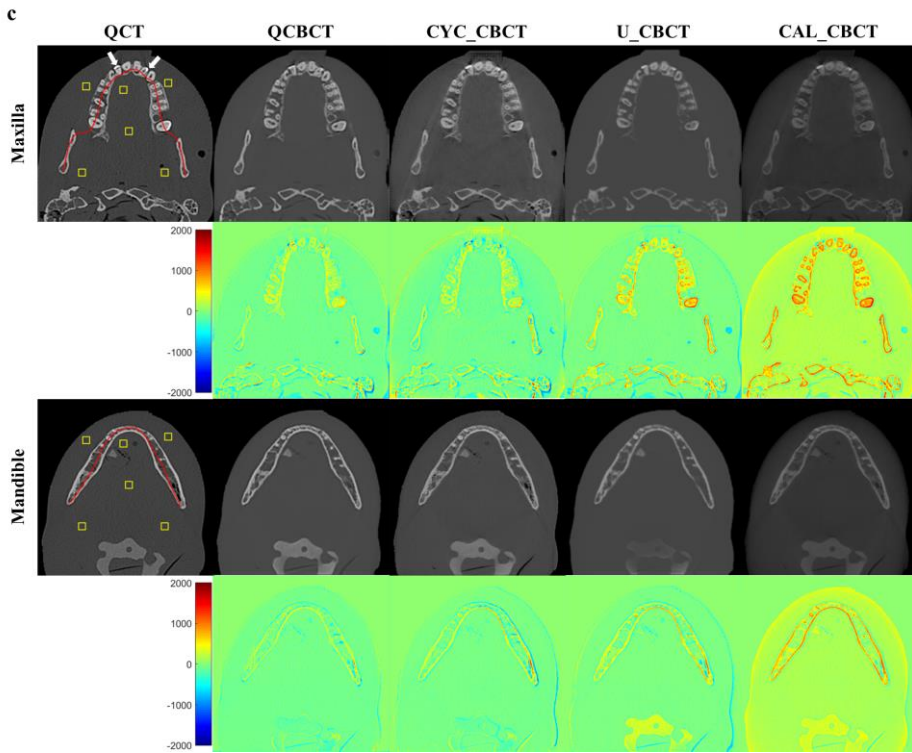
Figure 8. The axial slices of BMD images from the original QCT, their generations by deep learning methods (the first and third row), and their subtractions from the original QCT images (the second and fourth row) at the maxilla and the mandible. QCBCT produced by QCBCT-NET, CYC_CBCT by Cycle-GAN, U_CBCT by U-NET, and CAL_CBCT by only calibration from (a) training datasets under condition of 90 kVp and 10 mA, (b) test datasets under condition of 80 kVp and 8 mA, and (c) test datasets under condition of 90 kVp and 10 mA. The yellow squares shown in the QCT image were ROIs for calculation of the spatial nonuniformity (SNU), the red curve shown in the QCT image was the dental arch for BMD (voxel intensity) profiles, and the white arrows shown in the QCT images indicated the dental implant at the maxilla in (b), and the dental restorations at the maxilla in (c).
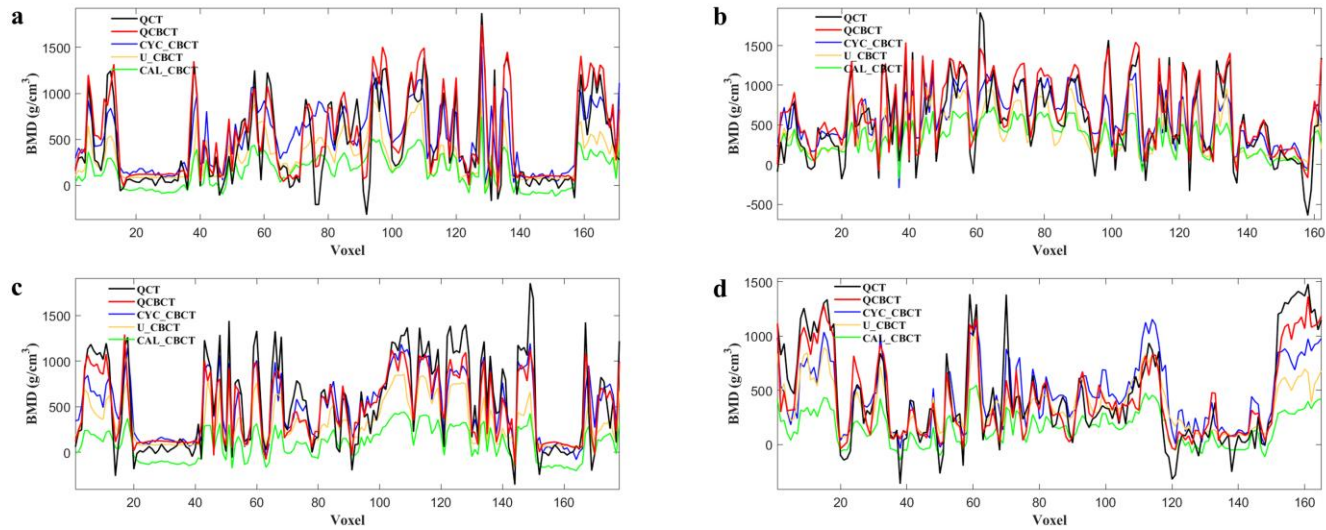
Figure 9. The BMD (voxel intensity) profiles along the dental arch at the maxilla and the mandible in the QCT, and QCBCT, CYC_CBCT, U_CBCT, and CAL_CBCT images shown in Figure 2. Pearson correlation coefficients of QCBCT, CYC_CBCT, U_CBCT, and CAL_CBCT with the original QCT were (a) 0.92, 0.65, 0.60, and 0.65, respectively, for the profile at the maxilla and, (b) 0.93, 0.70, 0.65, and 0.69, respectively, for the profile at the mandible shown in Figure 2(b), and (c) 0.92, 0.89, 0.84, and 0.88, respectively, for the profile at the maxilla, and (d) 0.93, 0.81, 0.82, and 0.82, respectively, for the profile at the mandible shown in Figure 2(c).
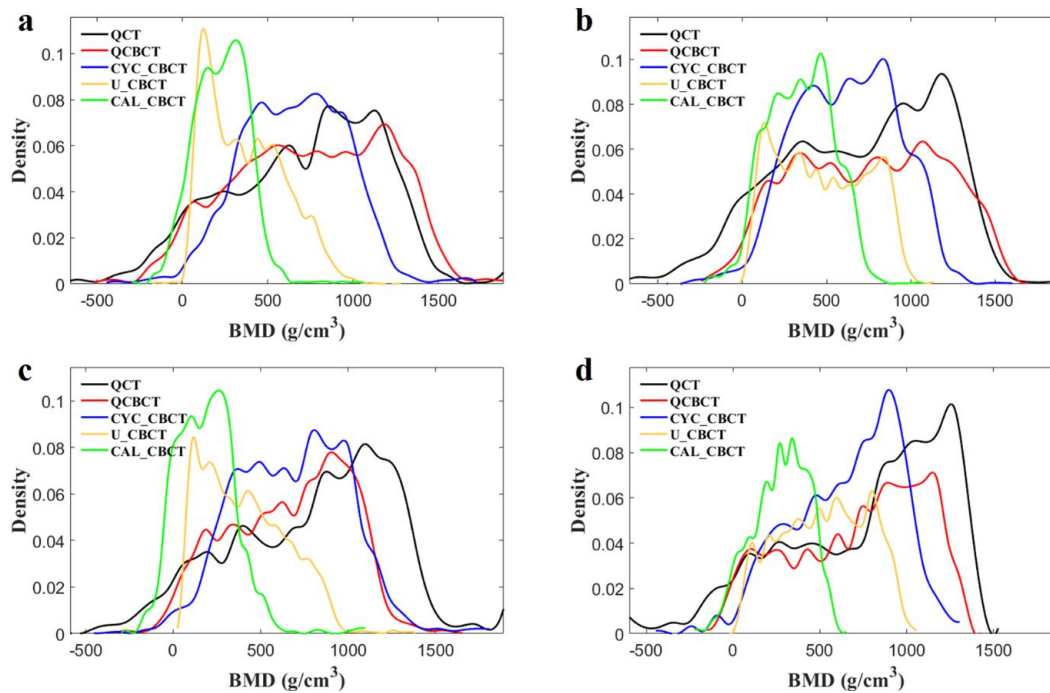
Figure 10. The BMD distribution in an axial slice of the original QCT, and QCBCT, CYC_CBCT, U_CBCT, and CAL_CBCT images. (a) CBCT images at the maxilla under condition of 80 kVp and 8 mA, (b) at the mandible under condition of 80 kVp and 8 mA, (c) at the maxilla under condition of 90 kVp and 10 mA, and (d) at the mandible under condition of 90 kVp and 10 mA.
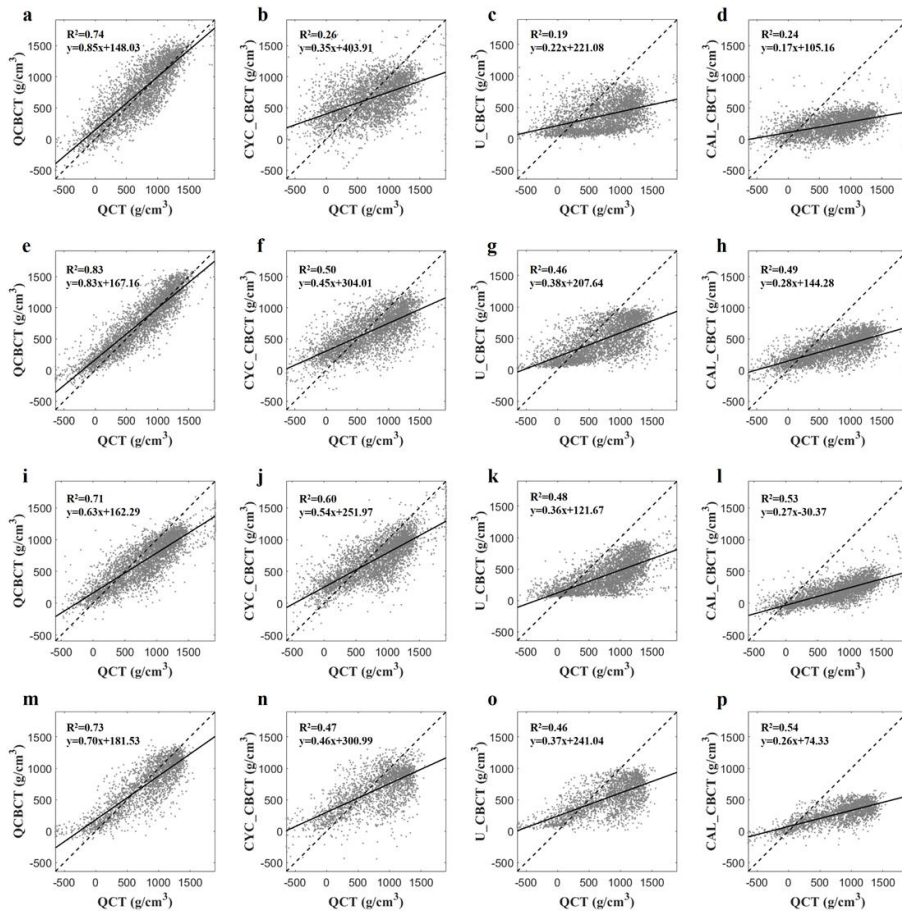
Figure 11. The linear relationships between the original QCT, and QCBCT, CYC_CBCT, U_CBCT, and CAL_CBCT images. (a)-(d) CBCT images at the maxilla under condition of 80 kVp and 8 mA, (e)-(h) at the mandible under condition of 80 kVp and 8 mA, (i)-(l) at the maxilla under condition of 90 kVp and 10 mA, and (m)-(p) at the mandible under condition of 90 kVp and 10 mA.
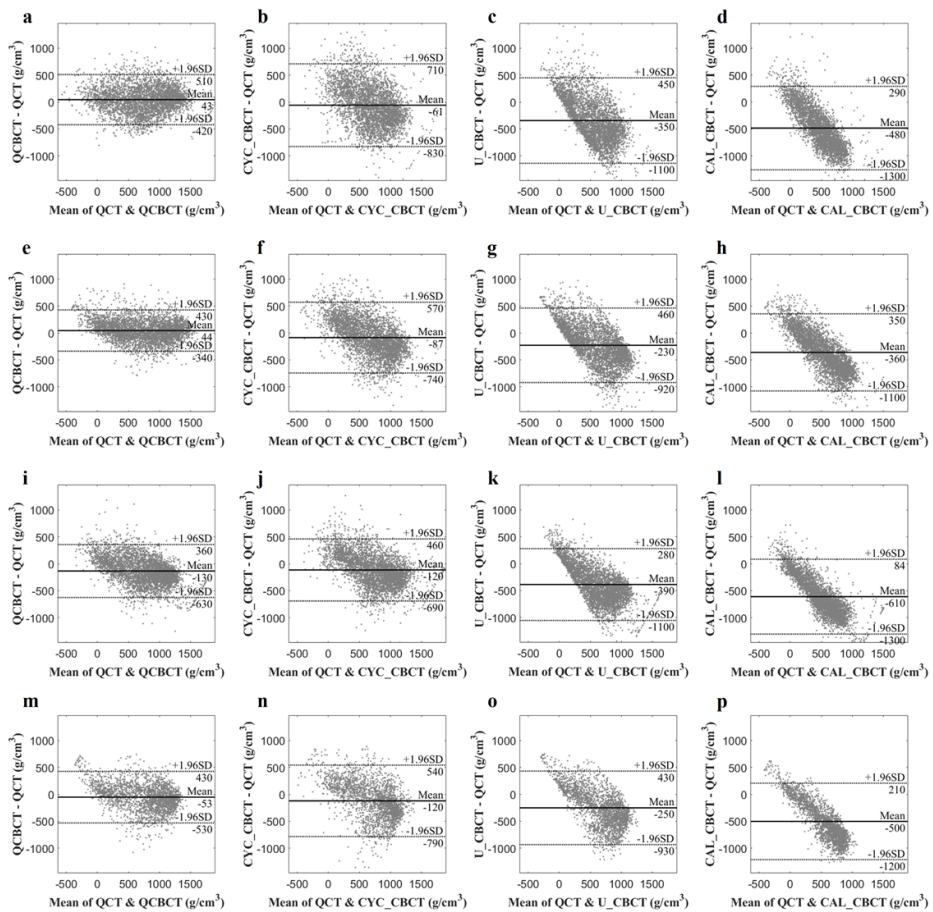
Figure 12. The linear relationships between the original QCT, and QCBCT, CYC_CBCT, U_CBCT, and CAL_CBCT images. (a)-(d) CBCT images at the maxilla under condition of 80 kVp and 8 mA, (e)-(h) at the mandible under condition of 80 kVp and 8 mA, (i)-(l) at the maxilla under condition of 90 kVp and 10 mA, and (m)-(p) at the mandible under condition of 90 kVp and 10 mA.

36

DISCUSSION

We developed a hybrid deep-learning model (QCBCT-NET) consisting of Cycle-GAN and U-Net to quantitatively and directly measure BMD from CBCT images. The BMD measurements of QCBCT images produced by QCBCT-NET significantly outperformed the CYC_CBCT images produced by Cycle-GAN and U_CBCT images produced by U-Net at both the maxilla and mandible area when compared to the original QCT. We used paired training data in the Cycle-GAN implementation with the residual blocks, which forced the network to focus on reducing image artifacts and enhancing bone contrast, rather than focusing on bone structural mismatches. Through the residual blocks in the generator architecture of the Cycle-GAN, the network could learn the difference between the source and target based on the residual image and generate corrected bone images more accurately [52]. In a study, a Cycle-GAN was used to capture the relationship from CBCT to CT images while simultaneously supervising an inverse of the CT to CBCT transformation model [36]. The Cycle-GAN doubled the process of a typical GAN by enforcing an inverse transformation, which doubly constrained the model and

increased accuracy in the output images [38]. In our study, the Cycle-GAN can learn both intensity and textural mapping from a source distribution of the CBCT bone image to a target distribution of the QCT bone image.

In previous studies, U-Net architectures were used to directly synthesize CT-like CBCT images for their corresponding CT images especially on paired datasets [43, 44]. The U-Net could suppress global scattering artifacts and local artifacts derived from CBCT images by capturing both global and local features in the image spatial domain [43]. In addition, the spatial uniformity of CT-like CBCT images was enhanced close to those of corresponding CT images while maintaining the anatomical structures on the CBCT images [44]. Therefore, in our results, the spatial uniformity of CBCT images produced by U-Net was improved, but the contrast of the bone images was reduced when compared to the CYC_CBCT images by Cycle-GAN.

In our study, the two-channel U-Net, which learned spatial information of CBCTs and corresponding CYC_CBCT images simultaneously, could improve image contrast and uniformity by suppressing beam hardening artifacts and scattering noise [43]. The CYC_CBCT images out of the two inputs helped the U-Net to focus on learning pixel-wise correspondence (or

mapping) between QCT and CBCT images while maintaining the original intensity distribution of the bone structures. The combination loss of MAE and SSIM in the U-Net facilitated faster convergence and better accuracy considering the pixel-wise errors and structural similarity. As a result, the BMDs (voxel intensities) from the QCBCT demonstrated more accuracy than those from the CYC_CBCT and U_CBCT without regard to relative positions of the bone in the image volume [51], or effects from different radiation doses or scanning conditions used in clinical settings.

We combined the Cycle-GAN with the two-channel U-Net model to further improve the contrast and uniformity of the CBCT bone images. The Cycle-GAN improved the contrast of the bone images by reflecting the original BMD distribution of the QCT images locally, while the two-channel U-Net improved the spatial uniformity of the bone images by globally suppressing the image artifacts and noise. As a result, the Cycle-GAN and two-channel U-Net worked to provide complementary benefits in improving the contrast and uniformity of the bone image locally and globally. Consequently, the QCBCT-NET could substantially enhance the linearity, uniformity, and contrast as well as the anatomical and quantitative accuracy of the bone images in order to

quantitatively measure BMD in CBCT. Although the BMD linear relationships and agreement limits of QCBCT images were superior to those of CYC_CBCT and U_CBCT images, the accuracy of our method should be further improved for clinical applications.

Our study had some limitations. First, because paired CBCT and CT images were acquired at different imaging situations typically, the bone structures of the images were not perfectly aligned even after registration. Therefore, the registration error of CBCT and CT images might cause adverse impacts during network training. Second, our study had a potential limitation of generalization ability due to using a relatively small number of training dataset. Overfitting of the training CNN model, which resulted in the model learning statistical regularity specific to the training dataset, could impact negatively the model's ability to generalize to a new dataset [53]. Third, the results presented in this study were based on two human skull phantoms with and without metal restorations instead of actual patients. Our method needs to be validated for the dataset from actual patients having dental fillings and restorations for its application in clinical research and practice, and compared to the conventional scatter-based method in future studies.

CONCLUSIONS

We proposed QCBCT-NET to directly and quantitatively measure BMD from CBCT images based on a hybrid deep-learning model of combining the generative adversarial network (GAN) and U-Net. The Cycle-GAN and two-channel U-Net in QCBCT-Net provided complementary benefits of improving the contrast and uniformity of the bone image locally and globally. The BMD images produced by QCBCT-NET significantly outperformed the images produced by Cycle-GAN or U-Net in MAD, PSNR, SSIM, NCC, and linearity when compared to the original QCT. The QCBCT-NET substantially enhanced the linearity, uniformity, and contrast as well as the anatomical and quantitative accuracy of the bone images, and demonstrated more accuracy than the Cycle-GAN and the U-Net for quantitatively measuring BMD in CBCT. In future studies, we plan to evaluate the proposed method on the actual patient dataset to prove its clinical efficacy.

REFERENCES

1.   P. Ammann and R. Rizzoli. Bone strength and its determinants. Osteoporos Int 14 Suppl 3, S13-8 (2003).

2.   E. Seeman. Bone quality: the material and structural basis of bone strength. J Bone Miner Metab 26, 1-8 (2008).

3.   J. A. Kanis, et al. Assessment of Fracture Risk and Its Application to Screening for Postmenopausal Osteoporosis - Synopsis of a WHO Report. Osteoporosis Int 4, 368-381 (1994).

4.   M. J. Budoff, et al. Measurement of thoracic bone mineral density with quantitative CT. Radiology 257, 434-40 (2010).

5.   C. E. Cann. Quantitative CT for determination of bone mineral density: a review. Radiology 166, 509-22 (1988).

6.   H. Giambini, et al. The Effect of Quantitative Computed Tomography Acquisition Protocols on Bone Mineral Density Estimation. J Biomech Eng 137, 114502 (2015).

7.   J. E. Adams. Quantitative computed tomography. Eur J Radiol 71, 415-24 (2009).

8.   S. Rues, et al. Effect of bone quality and quantity on the primary stability of dental implants in a simulated bicortical placement. Clin Oral Investig 25, 1265-1272 (2021).

9.   I. Turkyilmaz and E. A. McGlumphy. Influence of bone density on implant stability parameters and implant success: a retrospective clinical study. BMC Oral Health 8, 1-8 (2008).

10.   T. Kiljunen, T. Kaasalainen, A. Suomalainen and M. Kortesniemi. Dental cone beam CT: A review. Phys Med 31, 844-860 (2015).

11. K. Kamburoglu. Use of dentomaxillofacial cone beam computed tomography in dentistry. World Journal of Radiology 7, 128-130 (2015).

12. D. Dalessandri, et al. Advantages of cone beam computed tomography (CBCT) in the orthodontic treatment planning of cleidocranial dysplasia patients: a case report. Head Face Med 7, 1-9 (2011).

13. S. D. Kapila and J. M. Nervina. CBCT in orthodontics: assessment of treatment outcomes and indications for its use. Dentomaxillofac Rad 44, 1-19 (2015).

14. J. P. Woelber, J. Fleiner, J. Rau, P. Ratka-Kruger and C. Hannig. Accuracy and Usefulness of CBCT in Periodontology: A Systematic Review of the Literature. Int J Periodontics Restorative Dent 38, 289-297 (2018).

15. D. G. Kim. Can Dental Cone Beam Computed Tomography Assess Bone Mineral Density? J Bone Metab 21, 117-126 (2014).

16. R. Pauwels, R. Jacobs, S. R. Singer and M. Mupparapu. CBCT-based bone quality assessment: are Hounsfield units applicable? Dentomaxillofac Radiol 44, 20140238 (2015).

17. P. Mah, T. E. Reeves and W. D. McDavid. Deriving Hounsfield units using grey levels in cone beam computed tomography. Dentomaxillofac Rad 39, 323-335 (2010).

18. R. Molteni. Prospects and challenges of rendering tissue density in Hounsfield units for cone beam computed tomography. Oral Surg. Oral Med. Oral Pathol. Oral Radiol 116, 105-19 (2013).

19. R. Schulze, et al. Artefacts in CBCT: a review. Dentomaxillofac Radiol 40, 265-73 (2011).

20.   A. Katsumata, et al. Relationship between density variability and imaging volume size in cone-beam computerized tomographic scanning of the maxillofacial region: an in vitro study. Oral Surg. Oral Med. Oral Pathol. Oral Radiol 107, 420-425 (2009).

21.   T. E. Reeves, P. Mah and W. D. McDavid. Deriving Hounsfield units using grey levels in cone beam CT: a clinical application. Dentomaxillofac Rad 41, 500-508 (2012).

22.   I. M. Silva, D. Q. Freitas, G. M. Ambrosano, F. N. Boscolo and S. M. Almeida. Bone density: comparative evaluation of Hounsfield units in multislice and cone-beam computed tomography. Braz Oral Res 26, 550-6 (2012).

23.   Y. Nomura, H. Watanabe, E. Honda and T. Kurabayashi. Reliability of voxel values from cone-beam computed tomography for dental use in evaluating bone mineral density. Clin Oral Implan Res 21, 558-562 (2010).

24.   M. Naitoh, A. Hirukawa, A. Katsumata and E. Ariji. Evaluation of voxel values in mandibular cancellous bone: relationship between cone-beam computed tomography and multislice helical computed tomography. Clin Oral Implan Res 20, 503-506 (2009).

25.   A. Parsa, et al. Reliability of voxel gray values in cone beam computed tomography for preoperative implant planning assessment. Int J Oral Maxillofac Implants 27, 1438-42 (2012).

26.   A. Parsa, N. Ibrahim, B. Hassan, P. van der Stelt and D. Wismeijer. Bone quality evaluation at dental implant site using multislice CT, micro-CT, and cone beam CT. Clin Oral Implan Res 26, E1-E7 (2015).

27.   J. Y. Cha, J. K. Kil, T. M. Yoon and C. J. Hwang. Miniscrew stability evaluated with computerized tomography scanning. Am J Orthod Dentofacial Orthop 137, 73-9 (2010).

28.   P. Z. Tao Xu, Qiuyuan Huang, Han Zhang, Zhe Gan, Xiaolei Huang, Xiaodong He. Attngan: Fine-grained text to image generation with attentional generative adversarial networks. arXiv preprint 1711.10485, 1-9 (2017).

29.   Y. Li, J. Garrett and G. H. Chen. Reduction of Beam Hardening Artifacts in Cone-Beam CT Imaging via SMART-RECON Algorithm. Medical Imaging 2016: Physics of Medical Imaging 9783, 97830W (2016).

30.   B. B. Bechara, W. S. Moore, C. A. McMahan and M. Noujeim. Metal artefact reduction with cone beam CT: an in vitro study. Dentomaxillofac Rad 41, 248-253 (2012).

31.   M. Wu, et al. Metal artifact correction for x-ray computed tomography using kV and selective MV imaging. Med Phys 41, 1-17 (2014).

32. L. Zhu, Y. Xie, J. Wang and L. Xing. Scatter correction for cone-beam CT in radiation therapy. Med Phys 36, 2258-68 (2009).

33. Y. Xu, et al. A practical cone-beam CT scatter correction method with optimized Monte Carlo simulations for image-guided radiation therapy. Phys Med Biol 60, 3567-87 (2015).

34. Q. Cao, Sisniega, A., Stayman, J. W., Yorkston, J., Siewerdsen, J. H., & Zbijewski, W. Quantitative cone-beam CT of bone mineral density using model-based reconstruction. Medical Imaging 2019: Physics of Medical Imaging 10948, 109480Y (2019).

35. C. Ledig, et al. Photo-realistic single image super-resolution using a generative adversarial network. arXiv preprint 1609.04802, 1-19 (2017).

36. J.-Y. Zhu, T. Park, P. Isola and A. A. Efros. Unpaired Image-to-Image Translation using Cycle-Consistent Adversarial Networks. Proceedings of the IEEE international conference on computer vision, 2223-2232 (2017).

37. X. Yi, E. Walia and P. Babyn. Generative adversarial network in medical imaging: A review. Med Image Anal 58, 1-20 (2019).

38. J. Harms, et al. Paired cycle-GAN-based image correction for quantitative cone-beam computed tomography. Med Phys 46, 3998-4009 (2019).

39. O. Ronneberger, Philipp Fischer, and Thomas Brox. U-net: Convolutional networks for biomedical image segmentation. In: International Conference on Medical image computing and computer-assisted intervention). Springer (2015).

40.   C. Tian. Deep Learning for Image Denoising: A Survey. In: International Conference on Genetic and Evolutionary Computing). Springer (2018).

41.   W. J. Do, et al. Reconstruction of multicontrast MR images through deep learning. Med Phys 47, 983-997 (2020).

42.   G. Liu. Photographic image synthesis with improved U-net. In: 2018 Tenth International Conference on Advanced Computational Intelligence (ICACI)). IEEE (2018).

43.   L. Chen, X. Liang, C. Shen, S. Jiang and J. Wang. Synthetic CT generation from CBCT images via deep learning. Med Phys 47, 1115-1125 (2020).

44.   S. Kida, et al. Cone Beam Computed Tomography Image Quality Improvement Using a Deep Convolutional Neural Network. Cureus 10, 1-15 (2018).

45. J. W. Choi. Analysis of the priority of anatomic structures according to the diagnostic task in cone-beam computed tomographic images. Imagng Sci Dent 46, 245-249 (2016).

46. J. W. Choi, et al. Relationship between physical factors and subjective image quality of cone-beam computed tomography images according to diagnostic task. Or Surg or Med or Pa 119, 357-365 (2015).

47. J. M. Shin, et al. Contrast reference values in panoramic radiographic images using an arch-form phantom stand. Imagng Sci Dent 46, 203-210 (2016).

48. C. DH, et al. Reference line-pair values of panoramic radiographs using an arch-form phantom stand to assess clinical image quality. Imaging Sci Dent 43, 7-15 (2013).

49.   S. J. Lee, et al. Virtual skeletal complex model- and landmark-guided orthognathic surgery system. J Craniomaxillofac Surg 44, 557-68 (2016).

50.   D. G. Bailey and R. M. Hodgson. Range Filters - Local Intensity Subrange Filters and Their Properties. Image Vision Comput 3, 99-110 (1985).

51.   G. R. Swennen and F. Schutyser. Three-dimensional cephalometry: spiral multi-slice vs cone-beam computed tomography. Am J Orthod Dentofacial Orthop 130, 410-6 (2006).

52.   K. He, X. Zhang, S. Ren and J. Sun. Deep residual learning for image recognition. the IEEE conference on computer vision and pattern recognition, 770-778 (2016).

53.   O. Kwon, et al. Automatic diagnosis for cysts and tumors of both jaws on panoramic radiographs using a deep convolution neural network. Dentomaxillofac Rad 49, 1-9 (2020).

국 문 초 록

골밀도 측정을 위한

적대적생성신경망 기반 정량적

CBCT 측정

용태훈

응용바이오공학전공

서울대학교 융합과학기술대학원

골다공증은 골의 밀도가 낮아 쉽게 골절되는 골격계

질환이며, 골다공증은 그 자체만으로는 거의 증상을 일으키지 않고

뼈가 부러져서 골다공증을 발견하게 되는 경우가 많다. 골다공증을 진단하고 향후 골절 위험을 예측하기 위한 방법으로 골밀도(bone mineral density)를 측정하는 방법이 있다. BMD 측정은 사람의 골의 밀도를 추정하는 직접적인 방법이고, 정확한 골의 밀도 측정은 매우 중요하다.

골밀도를 측정하기 위해서는 CT 스캔 시, 골밀도 팬텀을 함께 스캔한 후, QCT 방법을 사용하여 CT 영상의 Hounsfield Units 으로부터 BMD 를 정량적으로 계산하게 된다. 환자와 함께 촬영한 골밀도 BMD 팬텀을 통해 Hounsfield Units 과 BMD 간의 선형 관계를 측정함으로서 평가할 수 있다. 최근 CBCT 는 MDCT 에 비해 낮은 방사선량과 짧은 획득 시간, 그리고 더 높은 해상도 등 다양한 장점을 포함하여 많은 이점을 제공하기 때문에 치과 치료 및 계획에 널리 사용되고 있지만, CBCT 시스템의 복셀값은 임의적이며 정확한 HU 를 구할 수 없으므로 골밀도에 대한 평가를 허용하지 않는 단점이 있다. CBCT 로부터 정확한

BMD 를 측정하기 위해서는 균일하고 정확한, 높은 퀄리티의 CBCT 영상을 필요로 한다.

본 연구에서는 적대적 생성 신경망(Cycle-GAN)과 인코더 및 디코더 구조의 U-Net 을 결합한 하이브리드 딥러닝 모델(QCBCT-NET)을 기반으로 골 영역의 선형성과 균일성을 향상시켜 Cone-beam CT(CBCT) 영상에서 BMD 를 직접적 그리고 정량적으로 측정하며, QCBCT-NET 에 의해 선형성과 균일성이 강화된 골 이미지와 기존의 영상 생성 분야에서 state-of-the-art 를 기록한 Cycle-GAN 및 U-Net 에 의해 강화된 골 영상을 비교하였다. 아크릴로 둘러싸인 인간 두개골의 두 팬텀을 사용하였고, 하나는 훈련 및 검증 데이터 세트로서 금속 수복물이 없는 팬텀이고, 다른 하나는 테스트 데이터 세트용으로서 금속 수복물을 포함하여 영상의 잡음을 발생시키는 팬텀이다. 우리는 QCT(quantitative CT)와 CBCT 이미지의 짝을 이룬 학습 데이터를 사용하여 잔차(residual) 블록을 포함하는 Cycle-GAN 과 다중 채널 U-Net 으로 구성된 QCBCT-NET 을 제안하였다.

QCBCT-NET 에 의해 생성된 BMD 이미지는 평균 절대차(MAD), 최대 신호 대 잡음비(PSNR), 정규화된 교차 상관 계수(NCC), 구조적 유사성(SSIM) 그리고 선형성(linearity)에서 Cycle-GAN 또는 U-Net 에 의해 생성된 이미지보다 훨씬 우수한 성능을 보였다. QCBCT-NET 은 Cycle-GAN 을 사용하여 QCT 영상의 원래 BMD 분포를 국부적으로 반영하여 골 영상의 대비도(contrast)를 향상시켰고, 다중채널 U-Net 을 사용하여 영상 잡음과 노이즈를 전역적으로 억제하여 골 영상의 공간적 균일성(uniformity)을 향상시켰다. QCBCT-NET 은 골 영상의 해부학적 및 정량적 정확도뿐만 아니라 선형성, 균일성, 대비도를 크게 향상시켰으며 CBCT 에서 BMD 를 정량적으로 측정하는 Cycle-GAN 및 U-Net 보다 더 높은 정확도를 보여주었다.

주요어 : 골밀도, 정량적 CBCT, 딥러닝, 적대적생성신경망, U 자형 신경망

학 번 : 2019-23327